Nanopolycrystalline Materials;
A General Atomistic Model for Simulation

Dean C. Sayle[1*], Benoît C. Mangili[1], David W. Price[3] and Thi X. Sayle[1]

[1]*Department ofApplied Science, Security & Resilience, Cranfield University, Shrivenham, SN6 8LA, UK, Department of Applied Science, Security & Resilience, Cranfield University, Shrivenham, SN6 8LA, UK,*

[2]*Material Science Research Division, Research and Applied Science, AWE, Aldermaston, RG7 4PR, UK, and Department ofApplied Science, Security & Resilience, Cranfield University, Shrivenham, SN6 8LA, UK*

[*]E-mail: d.c.sayle@cranfield.ac.uk

ABSTRACT

We present a general strategy for generating full atomistic models of nanopolycrystalline materials including bulk and thin film. In particular, models for oxide nanoparticles were constructed using simulated amorphisation and crystallisation and used to populate a library of oxide nanoparticles (amorphous and crystalline) with different radii. Nanoparticles were then taken from this library and positioned, within a specific volume, using Monte Carlo techniques, to facilitate a tight-packed structure. The grain size distribution of the polycrystalline material was controlled by selecting particular sized nanoparticles from the library. The (randomly oriented) grains facilitated a polycrystalline oxide, which comprised a network of general grain-boundaries. To help validate the model, gas diffusion through the (polycrystalline) oxide material was then simulated and the activation energy calculated *directly*. Specifically, we explored He transport in UO_2, which is an important material with respect to both civilian and military applications. We found that He transport proceeds much faster through the grain-boundary and grain-junction network compared with intracrystalline UO_2 regions, in accord with experiment.

INTRODUCTION

The properties of a material are influenced profoundly by its microstructure, which includes, for example, grain-boundaries, dislocations and point defects. Accordingly, if we are to generate atomistic models, which are sufficiently realistic in that they can be used to *directly* calculate properties or simulate processes with sufficient accuracy to be of benefit to experiment, then a strategy for introducing such microstructures into a model is required. Here, we present a general strategy for constructing full atomistic models of polycrystalline materials with controllable grain-size distributions and defect concentration. Our atomistic model comprises general grain-boundaries, dislocations (screw, edge and mixed) and point defects. Moreover, all the microstructural features are introduced into a single atomistic model such that the model can be used to calculate properties or simulate process directly. In particular, the synergistic interactions between microstructural features and how much this modifies the individual microstructures, is captured within the model. For example, the misfit strain energy associated with (near coincident [1]) matching of two misaligned oxide grains to form a general grain-boundary and how this impacts upon the atomistic structure of a neighbouring dislocation will be implicit within the model. We develop the method for polycrystalline UO_2 as a model system and explore how the microstructure influences He diffusion. This will help validate the model because experimental data pertaining to He diffusion in polycrystalline UO_2 is available.

Uranium is an important material with respect to both civilian and military applications. However, a major challenge for this material is to ensure its safe storage. In particular, water (vapour) in the surrounding air can adsorb onto the uranium surface forming hydrogen when it oxidises the uranium. This hydrogen forms uranium hydride UH_3 which is pyrophoric [2,3]. When open to the atmosphere, this reaction is an intermediate for the formation of UO_2, recycling the hydrogen. Conversely, when stored in a sealed canister, the uranium will consume all the oxygen (from air or vapour) for its oxidation, producing hydrogen gas, which can diffuse through the oxide layer, and reach the underlying metal, forming hydride. Without oxygen available, the system remains stable. Conversely, the opening of the canister furnishes a large quantity of oxygen, which can react catastrophically with the accumulated UH_3 [4,5] causing a safety hazard. Clearly, an understanding of the structure and gas diffusion in UO_2 is key to predict long-term storage properties. The diffusion of gas along grain boundaries can be many orders of magnitude higher compared with diffusion in the bulk materials. Accordingly, if one is to calculate accurately gas diffusion, the atomistic model must include structural defects including: grain-boundaries, dislocations, point defects. Experiments, performed on uranium and its oxides, are expensive, dangerous and difficult and therefore atomistic computer simulation offers a comparatively inexpensive and safe alternative. Indeed, UO_2 has enjoyed much attention. Specifically, Catlow and co-workers explored the diffusion of neutral gas species, helium or xenon, which are sub-products from nuclear reactions, in the

defective form of the oxide UO_{2-x} [6,7,8,9,10]. More recently, Price et al. explored diffusion along high-symmetry perfect grain-boundaries and calculated the diffusion coefficient along (110)/(221) [11].

Early studies of polycrystalline oxide materials considered high symmetry (twist/twin) grain-boundaries in isolation [12,13,14,15], which were generated using symmetry operators acting upon the crystal structure. The models were used to calculate diffusion coefficients and activation energies of (ionic) transport through boundary regions compared with mobility inside the grain. Model polycrystalline structures comprising general grain boundaries can also be generated using a Voronoi Construction, for example see ref. [16] This method also has the potential to control the size distribution of grains by careful choice of grain centres. Later, approaches used by Philpot and co-workers considered generating polycrystalline materials (bulk and thin film) using seeded crystallization [17]. This approach also enabled a degree of control over the grain-size distribution and relative orientation of the grains. Specifically, the grains were rotated about an axis normal to the surface enabling the atomic planes to be parallel. Such “evolutionary" simulations [18] promise to deliver more realistic models because they have the potential to capture within the model structural features that evolve during a real crystallization. Similar to the seeded crystallisations performed by Phillpot and co-workers a “Simulated amorphisation and crystallisation" strategy was developed to facilitate “spontaneous" crystallization [19]. Specifically, the strategy does not require (or indeed allow) the simulator to initiate or template the crystallisation using a precrystallised (artificial) nucleating seed; rather, the nucleating seed is allowed to spontaneously evolve, which was argued to be more realistic than using an “artificial" nucleating seed. A drawback of this method is that the nucleating seed can take a long time to evolve or indeed may never evolve and therefore this method is computationally expensive. A strategy for generating models of nanomaterials by positioning (model) nanobuilding blocks at “crystallographic positions” can be found in reference [20] and a review of nanocrystalline materials in ref. [21] A definitive text exploring interfaces in crystalline materials is available [22].

Our aim is to generate general models of polycrystalline materials (bulk and thin film). To achieve this we extended previous models. We generated oxide nanoparticles using simulated amorphisation and crystallisation. This was used to populate a library of oxide nanoparticles (amorphous and crystalline) spanning various radii. Nanoparticles were then taken from this library and positioned within a specific volume using Monte Carlo (MC) techniques to facilitate a tight-packed structure. The (randomly oriented) grains facilitated a polycrystalline oxide, which comprised a network of general grain-boundaries. Gas diffusion through the (polycrystallise) oxide material was then simulated and the activation energy calculated. Specifically, helium transport in UO_2 was used as a

model system. The chosen approach enables one to define the grain size distribution and defect concentrations of the model, the latter includes for example, dislocations, grain-boundaries and point defects. The approach comprises three steps:

- Generate a library of model nanobuilding blocks;
- Construct a nanopolycrystalline oxide with a pre-determined grain-size and defect distribution by selecting specific nanobuilding blocks from the library;
- Validate the method and test the structural model by simulating He diffusion in UO_2.

METHOD

In this section, we describe the potential models used to represent the interactions between atoms; the strategy used to generate models of the UO_2 nanoparticles that include microstructural features such as grain-boundaries, dislocations and point defects; the population of a database with atomistic models of UO_2 nanoparticles and finally the packing of nanoparticles, taken from the library, to formulate models for a nanopolycrystalline bulk or thin film.

Atomic Potentials

We used the DL_POLY code, which implements three-dimensional periodic boundary conditions, to perform all the molecular dynamical simulations in this study [23]. Effectively, the model for the crystalline bulk extends infinitely in all three spatial directions. However a gap was introduced to represent the free surface associated with the nanopolycrystalline thin film.

To describe the interaction between oxygen and uranium atoms, a rigid-ion model based upon a fully ionic description developed by Walker and Catlow [**Error! Bookmark not defined.**], was used; parameters to describe He - UO_2 interactions were taken from Grimes [9]. All the potential parameters used in this study are presented in table 1. We note that pseudo gas atoms (distinct from He and notated as PseudoGas in the present work) was used to impart pressure upon the system to promote crystallisation and therefore an arbitrary potential was employed. 'PseudoGas' atoms were described wholly by a repulsive model, avoiding any possibility of the gas crystallising.

Table 1

Generating Nanoparticles

In this section, we develop a procedure for simulating the atomistic structure of UO_2 nanoparticles. We then use the method to populate a library of nanoparticles with different diameters; Nanoparticles of uranium oxides have been synthesised experimentally [24].

Generating the full atomistic structure of a model nanoparticle is not trivial - realistic atomistic structures cannot easily be cut from the parent bulk material. For example, the morphological structure will comprise many low-energy surfaces. And although there are many simulation codes that use the crystal symmetry to generate an individual surface, for a nanoparticle one also needs to consider the structure of edges (where a pair of surfaces meet) and vertices (where three or more surfaces meet) together with the implications of dipolar surfaces and surface steps, corners and niche sites. In addition, for nanoparticles in excess of 10,000 atoms, the nanoparticles will likely comprise dislocations or (general) grain-boundaries [25,26]. Simulation strategies, to generate the structure of an individual dislocation or grain-boundary [27] within the bulk (perfect) material, are available. However, introducing a dislocation into the polyhedral structure of a nanoparticle is more of a challenge: Fabrication of a material experimentally inevitably involves some kind of crystallisation process. Indeed, crystallisation processes control the (micro) structure and hence the properties of the material. Moreover, by modifying the crystallisation process (whether crystallisation from solution, vapour deposition, molecular beam epitaxy, ball milling etc.) one can exact some control over the microstructure and hence the properties of the material. We propose therefore that the easiest way of capturing, within a single atomistic model, all the microstructural features observed experimentally, is to simulate the crystallisation process itself. Indeed, there are many theoretical studies that attempt to simulate the crystallization process. For example Piana and Gale performed some highly detailed MD simulations on the growth and dissolution of urea crystals [28]. Similarly, Hamad *et al.* used MD to explore the embryonic stages of ZnS nanobubbles [29]. These elegant dynamical atomistic simulations capture many of the important structural features associated with the nucleation, growth and dissolution processes. Indeed, these approaches would prove ideal in generating models for nanoparticles. Unfortunately, these approaches would also prove computationally too expensive (at present) to use to generate models for oxide nanoparticles comprising, for example, 50,000 atoms directly. Accordingly, we use simulated amorphisation/melting and crystallisation. This method has been used previously to generate realistic models of fluorite-structured oxide nanoparticles in quantitative agreement with experiment [30,31] and therefore we have confidence in applying the strategy to generate models of UO_2 nanoparticles.

Amorphisation

To amorphise/melt a UO_2 nanoparticle, we cut a cube comprising six {100} surfaces from the parent (fluorite-structured) material and tensioned the cube by 25% to effect amorphisation [32]. However, upon simulating the system using MD at high temperature, the simulations failed catastrophically. It was determined that the surface dipoles (fluorite {100} are dipolar type III surfaces [33]) together with the high configuration energy associated with corners and edges resulted

in considerable forces acting upon surface atoms. Consequently, the atoms underwent enormous accelerations and were subsequently vaporized from the surface. To help quench the surface dipoles, a simple code to cleave the (dipolar) surfaces while maintaining stoichiometry (fig. 1) was written. Using these cleaved nanoparticles, MD simulation, performed at high temperature, was successful in amorphising/melting the nanoparticles without catastrophic failure.

Fig. 1

Crystallisation

The next step was to crystallise the nanoparticle. Here, we applied MD simulation, performed at reduced temperatures, on the amorphous/molten nanoparticles. We considered a variety of different temperatures together with long (in this context nanosecond) running times. However, we were unsuccessful in facilitating crystallisation under such conditions. Accordingly, to increase the probability of a nucleating seed spontaneously evolving within a nanoparticle, a high pressure was imposed upon the system, which facilitated the evolution of nucleating seeds. This strategy follows our previous study on high-pressure crystallisation of TiO_2 nanoparticles [[34]]. Specifically, pressure was imparted by introducing a hard sphere gas (PseudoGas) into the simulation box; potential parameters are given in table 1. The nanoparticles were successfully crystallised under high-pressure.

Populating a Library of Nanoparticles

Amorphisation and crystallization was used to populate a library of UO_2 nanoparticles comprising seven nanoparticle sizes: 110,571 atoms (14 nm), 26,364 atoms (9 nm), 8,748 atoms (6 nm), 6,144 atoms (5 nm), 2,592 atoms (4 nm), 1,500 atoms (3 nm) and 768 atoms (2.5 nm). The next step was to use the nanoparticles as (secondary) building blocks and aggregate them together to form nanopolycrystalline structures.

Generating atomistic models for nanopolycrystalline bulk and thin film

Simulating (atomistically) the aggregation of several nanoparticles, each comprising up to 110,000 atoms, proved computationally prohibitive using available computational facilities. Consequently, to reduce computational expense, each nanoparticle was represented by a sphere, which was centered on the geometrical centre of the nanoparticle with a radius adjusted to enclose all the atoms comprising the nanoparticle within a minimum volume. The spheres were then represented using a simplified pair-potential, following equations (1), to reduce considerably the computational cost of simulating the aggregation:

$$U(d) = -\alpha \frac{\sqrt{R_1 \times R_s}}{\sqrt{d - (R_1 + R_2) + 1}} \qquad d > (R_1+R_2)$$

$$U(d) = \infty \qquad d \leq (R_1+R_2) \qquad (1)$$

where $U(d)$ is the interaction energy, d is the interatomic separation between spheres 1 and 2, α is an empirical coefficient, which was used to help increase the speed of the simulation and in this study was set to 0.1. R_1 and R_2 are the radii of spheres 1 and 2 respectively. The numerator contains the product of the radii of the two spheres involved in this pair-potential, which was designed to reduce the attraction between small spheres.

To achieve a high packing density, spheres with particular sizes to effect a particular grain-size distribution, were introduced randomly at the top or bottom of the simulation cell. Once inside the box, the spheres feel the attractive influence of one another and MC was used to direct them into low energy configurations. An additional potential, equation (2), was included to attract the spheres to a plane in the centre of the simulation cell:

$$V(x,y,z) = -\beta|z| \qquad (2)$$

where V(x,y,z) is the potential at a point (x,y,z) and β an emprirical parameter. Here, we used β=4, which was sufficient to draw the nanoparticles close to the plane at the centre of the cell relatively quickly, but not too strong as to deleteriously influence the packing. When generating a model for a polycrystalline bulk, the simulation was stopped when the box was full, fig. 2. Similarly, when simulating a model for a polycrystalline thin film, the simulation stopped and no further nanoparticles were added upon reaching the desired film thickness. MC simulations were run typically, for about a million steps to facilitate close packed configurations. The spheres were then replaced by the corresponding nanoparticles to obtain an atomistic model of a polycrystalline thin-film and polycrystalline bulk. A final, fully atomistic, MD simulation was performed on each system; pressure was imposed to compact further the nanocrystals and help fill void space. For the polycrystalline thin-film pressure was imparted using PseudoGas atoms.

Fig. 2

He diffusion in Nanopolycrystalline UO_2

The final step was to validate the atomistic models by simulating helium diffusion in polycrystalline

UO_2 using the model structures and comparing with experiment. To this end, He atoms were introduced into the polycrystalline UO_2 matrix. However, He atoms cannot be positioned at random into the matrix because they could inadvertently locate too close to oxygen or uranium positions, which would result in catastrophic failure of the MD simulation. To prevent this, we designed a simple algorithm to position the gas atoms into the UO_2 matrix. In particular, the algorithm searches for a suitable space to position the gas atoms. To achieve this, a position was chosen at random and the nearest-neighbour atoms (as determined by a distance less than a predefined value) surrounding this position are listed. The code then calculates the barycentre of these atoms. If all the atoms in the UO_2 matrix and previously introduced He atoms are sufficiently far away from this point, a He atom is added. By adjusting two parameters (nearest neighbour and distance from barycentre to nearest neighbour) we were able to control the introduction of the He into grain-boundary regions and/or bulk crystalline regions. For example, inter-crystalline (grain boundary) regions are generally less dense than intra-crystalline regions. Once all the He atoms were introduced into the oxide matrix, molecular dynamics (MD) was used to simulate the diffusion. The first step was a pseudo energy minimization; constant pressure MD was performed at 300 K, followed by equilibration to the desired temperature. Specifically, NPT (constant Number of atoms, Pressure and Temperature) MD simulation with a Hoover barostat and thermostat was performed, for 10 ps at zero pressure; a small timestep (0.1 fs) was needed to facilitate system stability, which was followed by equilibration for 50 ps with a 3 fs timestep. Once the potential energy associated with introducing the He had transformed to kinetic energy and extracted by the thermostat, NVT (constant Number of particles, Volume, Temperature) MD simulations were performed at different temperatures to facilitate data points which could be fitted to an Arrhenius relationship. We note that the MD system was stable using a maximum timestep of 3fs.

RESULTS

In this section we describe a typical simulation that facilitated the successful generation of models of oxide nano-crystals, we then present the atomistic structure of a range of nanocrystals.

Amorphisation/Melting

A cube of fluorite-structured UO_2, was cut (with {100} surfaces) from the parent bulk material and tensioned by 25%. This cube was then placed into a simulation box, with three-dimensional periodic boundaries, which were sufficiently large to prevent any interaction between the atoms and their periodic images. The corners of the cube were cleaved to help reduce the surface dipoles (fig. 3(a)). The nanoparticle comprised 8,788 uranium and 17,576 oxygen atoms. A PseudoGas was then introduced to impart pressure upon the nanoparticle. Constant pressure MD simulation was performed at 6,000 K under 20 GPa pressure for 500 ps, which resulted in an amorphous/molten nanoparticle (figs.

3(b) & 3(c)). Constant pressure and temperature was maintained using a Hoover thermostat and barostat [35] with 1.0 ps relaxation times.

Fig. 3

Crystallisation

To facilitate the crystallisation, the temperature was reduced to 3,000 K and constant pressure MD simulation was performed under 20 GPa pressure for 800 ps. The nanoparticle was then cooled; NVT MD simulation was performed at zero pressure (gas removed) at 300 K for 800 ps, followed by NVT MD at 0 K; the latter acts effectively as a pseudo energy minimisation. The final model structure is shown in Figs. 3(d) & 3(e). This general procedure was then used to populate the library of UO_2 nanoparticles.

Heat of Crystallisation

The configuration energy, calculated as a function of time during the crystallisation, is reported in Fig. 4. Initially, the energy, associated with the amorphous configuration, drops as the nanoparticle crystallises. Nucleating seeds spontaneously evolve within the amorphous nanoparticle and facilitate crystallisation of the amorphous ions surrounding the seed, emanating radially from each seed. After all the amorphous ions have been consumed (fully crystallised), the gradient reduces. The energy difference between the start and final configuration reflects, in part, the heat of crystallisation. We note the sudden drop in energy near 200 ps was attributed the annihilation of grain boundary where two neighbouring grains sinter into a single grain. This was determined by observing an animation of the process, which was generated using molecular graphical techniques. We note that the energy associated with the heat of crystallization was extracted via a thermostat to prevent the seed, which spontaneously evolves, from re-amorphising.

Fig. 4

U-U and O-O Radial Distribution Functions (RDF) calculated for the starting, amorphous and final UO_2 nanoparticle structure are shown in fig. 5. Inspection of the RDF trace reveals a crystalline starting configuration, which then broadens, indicating no long range order - indicative of an amorphous or molten material. The final RDF are much sharper than the amorphous material although not as sharp as the starting configuration. This is because the final structure includes: surface (interface) relaxation, defects (vacancies/interstitials) and extended defects including dislocations and grain-boundaries. The calculated RDF thus shows that the nanoparticle had amorphised completely with no residual crystallinity and successfully crystallised into the fluorite structure. The

lattice parameter, captured from the RDF, is 5.34 Å, which is within 3% of experiment (5.47 Å at 298 K) [36]). We note that the O-O RDF is consistent with Catlow [Error! Bookmark not defined.] and more recent work [37] who predicted that UO_2 was superionic. Molecular graphical techniques were then used to examine in more detail, the structural features.

Fig. 5

Atomistic Structure

Analysis of the atomistic structures revealed that the UO_2 had crystallised into the fluorite structure; experimentally, crystalline UO_2 nanoparticles with fluorite structure have been observed [38]. The structures of a variety of nanoparticles as a function of size are shown in table 2. Fig. 6 shows the morphological structure and microstructural features of four UO_2 nanoparticles, which are about 9 nm in diameter. Inspection of these nanoparticles reveal morphologies similar to the 'truncated octahedral' morphology of CeO_2 nanoparticles [31,32]. Specifically, {111} surfaces, which are the lowest energy surface [39], dominate the morphology, and are truncated by {100} surfaces, which, for fluorite-structured materials, are dipolar type (III). Here the surface dipole has been quenched via a rearrangement of atoms at the surface [33], fig. 6. Similar reconstructions have been observed previously in CeO_2 nanocrystals [32], Some nanoparticles present only {111} surfaces, fig. 7, although we note that they are not monocrystals.

Table 2

Fig. 6

Fig. 7

We note that the nanocrystals in fig. 6 are structurally non-identical yet were generated using identical simulation methodologies. This illustrates the random nature associated with the structure and evolution of nucleating seeds that spontaneously evolve. Specifically, the simulator does not have any influence over the structure; rather they evolve in a 'natural' way, which is a designed feature of the simulation strategy to help to generate more realistic models. In particular, the amorphisation & crystallisation strategy can be used to simulate structural distributions of nanoparticles that one would expect to observe experimentally. In addition, the model nanoparticles generated present several types of grain boundary and defect including: twin grain boundaries, fig. 8, fig. 9, screw dislocations, fig. 9, edge dislocations, fig. 8 and pinning defects, fig. 10.

Fig. 8

Fig. 9

Fig. 10

We also examined nucleating seed growth using molecular graphics. In particular, we observed that the nucleating seeds evolved at the surface of the nanocrystal exposing {111}. The seed then facilitated crystallisation, which emanated radially from the core, fig. 11. The figure also reveals two crystalline seeds, which evolve during the same time frame. It is interesting to note that the two grains reorient themselves prior to grain boundary formation, presumably to facilitate a higher symmetry twin boundary resulting in an energetically more stable structure. Specifically a twin boundary is energetically more stable than a lower symmetry general grain boundary because the latter is necessarily associated with a lattice misfit.

Molecular graphics was then used to examine the structure of the grain-boundary between two miss-oriented grains within a 9 nm nanoparticle and is shown in fig. 12(a). The grain boundary is clearly visible in the middle of the structure. To aid understanding, the volume occupied by the atoms have been calculated using a Connoly surface algorithm and reveals a reduced density of ions near the grain boundary in accord with grain-boundaries observed experimentally. We propose that a reduced ion density at boundary regions facilitates facile diffusion of helium, thus providing a pathway for helium transport. In the final section of this study, we will test this hypothesis by simulating He diffusion and linking He transport pathways with the atomistic structure and local ionic densities at boundary regions.

Nanopolycrystalline Structure

Once the library of nanoparticle models had been populated, the nanoparticle models were used to generate models for a nanopolycrystalline UO_2 thin film and a nanopolycrystalline UO_2 bulk. Computational facility limitations prevented us from using nanoparticles larger than 5 nm. However, the ability to explore polycrystalline materials with distributions comprising larger grain-sizes will be met in the future as computational facilities increase.

For the thin film, thirteen nanoparticles were introduced into the simulation cell, table 3. PseudoGas atoms were also introduced into the simulation cell to conduct the pressure. NPT MD simulation was then performed at 3,000 K for 392 ps at 5 GPa pressure. A segment of the thin film with surrounding gas atoms is shown in fig. 13. For the bulk system, twenty one nanoparticles filled

the simulation cell and NPT MD simulation was performed under 5 GPa pressure at 2000 K for 733 ps. The system was then cooled to room temperature; zero pressure MD simulation was performed for 50 ns at 300 K.

Table 3

Fig. 11

Fig. 12

Fig. 13

Thin Film

Inspection of the final nanopolycrystalline thin film structure, figs. 13, 14, reveals that it is similar to the starting configuration, but with the voids between the nanoparticles compacted. One can observe, fig. 13, that the larger grains are still present. However, some of the smaller grains have been consumed by sintering into a larger grain. It is also clear from the models that the intersection of multiple (miss-oriented) nanoparticles facilitates models of general grain-boundaries, which are important features. In particular, it is likely that He will diffuse predominantly along general grain-boundaries. We also note that some of the gas atoms are trapped inside the polycrystalline slab, fig. 13(c). This is a valuable feature of our model because nanopolycrystalline materials, such as UO_2 incorporate voids within their structure and will likely influence the transport of gas atoms. Our strategy therefore facilitates the introduction of such voids into the atomistic model.

Fig. 14

Bulk

Similar to the thin film, the model for polycrystalline bulk UO_2, fig. 15, comprises a variety of miss-oriented grains, separated by general grain boundaries and grain junctions, fig. 16. In addition, microstructural features include dislocations and point defects including vacancies.

Fig. 15

Diffusion

The models of polycrystalline structures, generated above, enable the activation energy for gas diffusion in a material containing a rich variety of defects to be calculated *directly*. In this section, we simulate He diffusion using the model of the polycrystalline bulk, fig. 15. The trajectories of the

He atoms, calculated during MD simulation performed at 1200 K, are presented in Fig. 17. Inspection of the data, reveals fast moving He ions, which traverse through the structure along grain-boundary regions. Conversely, those He ions within UO_2 crystalline grain interiors are comparatively immobile and remain trapped throughout the duration of the MD simulation.

Fig. 16

Fig. 17

The activation energy, associated with He diffusion, was calculated to be 0.2 eV and was extracted from the MSD data by fitting to a Arrhenius relationship following ref. [40]

Discussion

As the grain size increases, so the grain/grain-boundary (volume) ratio decreases [41]. Transport processes such as diffusion can be influenced by many factors including: grain boundaries, voids, defects, dislocations. Accordingly, if one is to calculate diffusion through a polycrystalline material directly, then the atomistic model needs to include all these structural features, including their synergy of interaction. Here, our atomistic models, fig. 15, are similar to those observed in polycrystalline UO_2 by Roudil and co-workers [42] although we note that the individual grain sizes within our models are smaller than experiment.

Previously Kadau and co-workers have generated polycrystalline materials by assembling spherical nanoparticles and compressing them into a close packed configuration [43]. Our study extends this approach to include oxide nanoparticles. In addition, the nanoparticles used in this present study are more realistic in that they comprise a variety of microstructural features including dis-locations, point defects, grain-boundaries, surface morphology including dipolar surface recon-structions. Accordingly, our strategy enables one to fine-tune the defect character. For example, if one desired a polycrystalline material with a high dislocation content, one could select nanoparticles from the library, which comprised dislocations traversing through their structure, rather than choosing from the library single crystal nanoparticles.

Computational limitations preclude simulating microscopic grains. Typically we would need to include billions of atoms. Nevertheless, we have captured, within a single structural model, all the important structural features observed experimentally including: miss-oriented crystalline grains separated by grain-boundaries and triple junctions, dislocations and point defects, which enables us to simulate He diffusion directly. As computational resources continue to increase in the future, it will be

possible to construct models of polycrystalline materials with wider grain size distributions and comprising larger grains. Specifically, in this study we were not able to use 6, 9 and especially 14 nm UO_2 nanoparticles.

We used a rigid ion model to simulate the diffusion of He in UO_2, which includes transport through, for example, grain-boundary regions and in close proximity to vacancies and dislocations. Clearly, such defects will impact upon the polarisation of the He and therefore it is desirable to use the shell model [44]. However, accommodating all the important microstructural features within a single simulation cell including their synergy of interactions to enable He transport to be simulated directly, necessitated a large simulation cell. Typically each diffusion simulation required 7 days using 128 processors (Intel® Xeon® 5160 (3.0 Ghz) Quad-Cores). Introducing the shell model would, we estimate, require one to two orders of magnitude more cpu, which is prohibitive at present; rather the focus of this present study was the development of a simulation strategy to explore gas diffusion directly in a full *microstructural* model together with model validation using the He/UO_2 system. Moreover, the activation energy barrier associated with He migration between interstitial sites via an oxygen or uranium vacancy was calculated to be 0.38 and 0.24 eV respectively using a shell-model description [9], which are similar to 0.2 eV calculated in this present study.

The calculated activation energy barriers are about ten times lower than that measured by Roudil and coworkers, who determined a value of 2 eV [42]. However, we note that Helium diffusion is measured using nuclear reaction analysis [45], which is not instantaneous and therefore cannot be conducted immediately after Helium implantation. Accordingly, only intragranular He would be measured experimentally using this technique because He present in grain-boundary regions would be lost owing to the (expected) much higher diffusion rate in these regions. Indeed, Guilbert and co-workers, in developing mathematical models to describe the diffusion, required the introduction of an additional component into the model to account for a 'fast' diffusion process. In particular, they proposed two hypotheses to explain the data: the influence of surface pores or intergranular diffusion. The latter, grain-boundary diffusion, 'would proceed at a far greater rate than (intragranular) diffusion' [46]. The work of Sauvage and co-workers [47] also highlights the importance of grain boundaries in the diffusion. Their analysis of the UO_2 system is compatible with the fast release of He through grain boundaries, together with slow intragranular diffusion.

Intragranular diffusion of He in UO_2 was calculated by Catlow and co-workers in 1990 to be 3.8 eV [9] using atomistic simulation and more recently 2.97 eV using density functional theory [48]; a value of 2.09 eV was determined using the thermally expanded lattice parameter of UO_2 at 1200K. Price calculated He diffusion along [321]-[221] Grain boundaries [11] and although this represented a

valuable extension to intergranular diffusion, 'real' diffusion will involve He mobility along a variety of (general) grain-boundaries. Our model better captures this behaviour because our calculated activation energy barrier is a sum over all the He atoms, which diffuse along various (dissimilar) general grain-boundaries.

CONCLUSION

We have developed a general strategy for simulating gas diffusion in nanopolycrystalline materials including bulk and thin film. In particular, we generated models for UO_2 nanoparticles using simulated amorphisation and crystallisation. Specifically, a nanoparticle is first amorphised and at a particular instance in time during the MD simulation, an amorphous crystalline seed spontaneously evolves in the amorphous nanocrystal, which nucleates crystallisation. In this study we crystallised the nanoparticles at high pressure to increase the probability of a nucleating seed evolving. This resulted in several nucleating seeds evolving within a single nanoparticle. Accordingly, as each seed propagated crystallisation, the crystallisation fronts impinged upon one another facilitating the evolution of grain-boundaries within the (single) nanoparticle.

This amorphisation and crystalisation strategy enables a variety of important microstructural features to be introduced into the model including, for example: (general) grain-boundaries, screw, edge and mixed screw-edge dislocations, point defects, including vacancies which pin the dislocations, nanocrystal morphologies including surfaces exposed (we observe $UO_2\{111\}$, $UO_2\{100\}$) the atomistic structures of edges and corners, together with surface steps, ledges and niche sites. Such microstructural features are difficult to introduce into a structural model using alternative means, for example with symmetry operators.

This method was then used to populate a library of UO_2 nanoparticles with different radii. Nanoparticles were taken from this library and positioned, within a specific volume using Monte Carlo techniques, to facilitate tight-packed structures. The (randomly oriented) nanoparticles facilitated a polycrystalline UO_2 matrix, which comprised a network of general grain-boundaries.

This general strategy facilitates the generation of atomistic models of (nano)polycrystalline materials with a predefined grain size distribution by taking the component grains from a library of model nanocrystals. The model of polycrystalline UO_2 was then used to simulate He transport through the material. The simulations enabled a direct calculation of the activation energy for gas diffusion in a material comprising a large range of defects.

Animations (ion trajectories during the MD simulation) of the He diffusing through the UO_2 matrix

revealed that He transport through the material proceeds fastest via (general) grain-boundary regions rather than intragranular regions and is associated with an activation energy barrier of 0.2eV.

Acknowledgement

This work was supported by AWE. We acknowledge the Cambridge-Cranfield High Performance Computing Facility for computational resources and EPSRC (GR/S4843 1/1, GR/S48448/0 1, and GR/S84415/01) for funding.

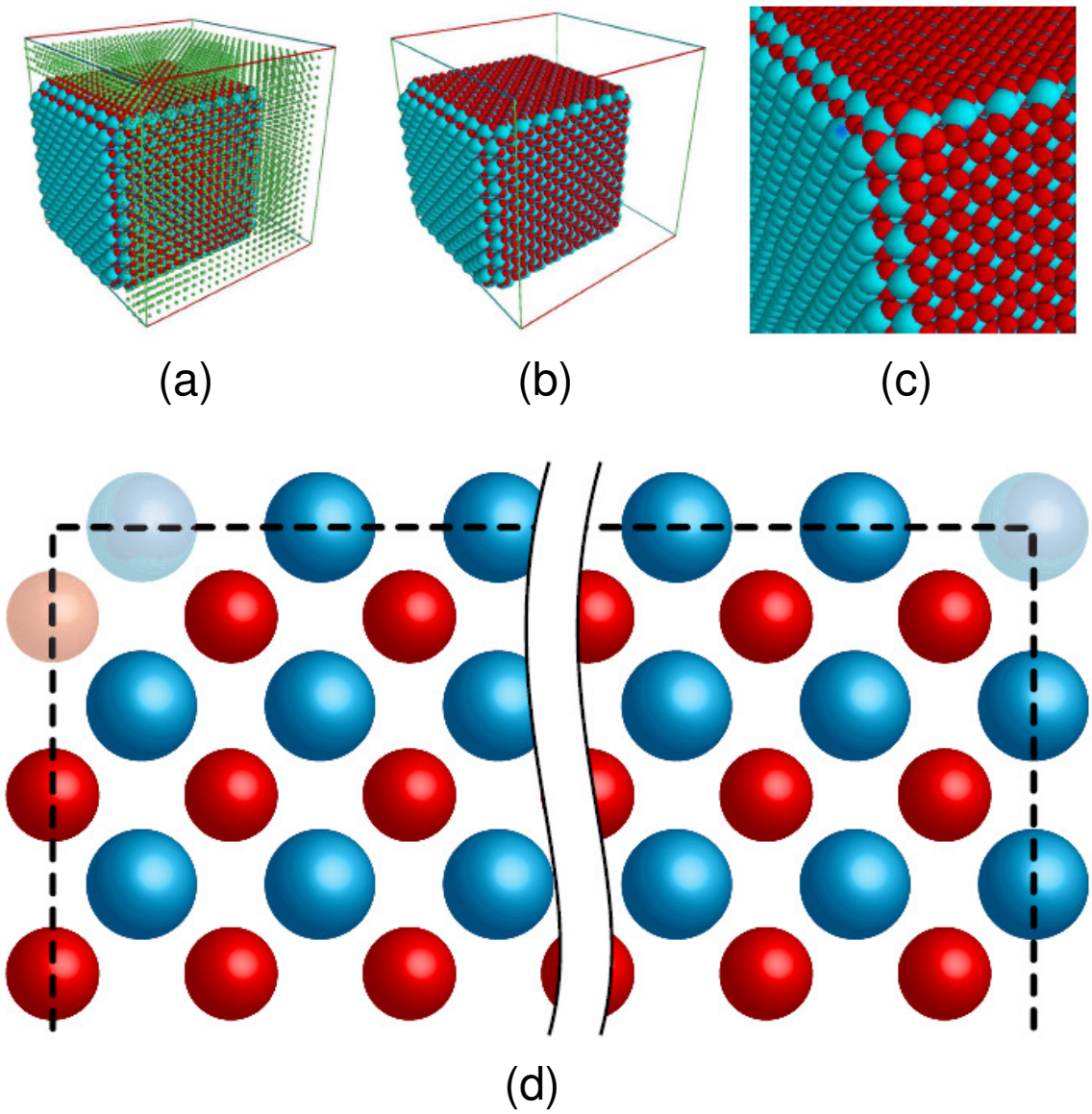

Figure 1: Sphere model representation of the atom positions comprising the UO_2 nanoparticle illustrating the truncation of a perfect cube of UO_2 used to help quench the surface dipole. (a) Perfect truncated cube in the simulation box together with the pseudo gas, at the start of the simulation. (b) shows the nanoparticle without the gas atoms to improve clarity of the figure and is enlarged in (c).

(d) is a schematic showing cleavage of two rows of atoms when the surfaces are different (top left corner) or one row when it connects two surfaces of the same atom type (top right corner). U is coloured blue and O is red.

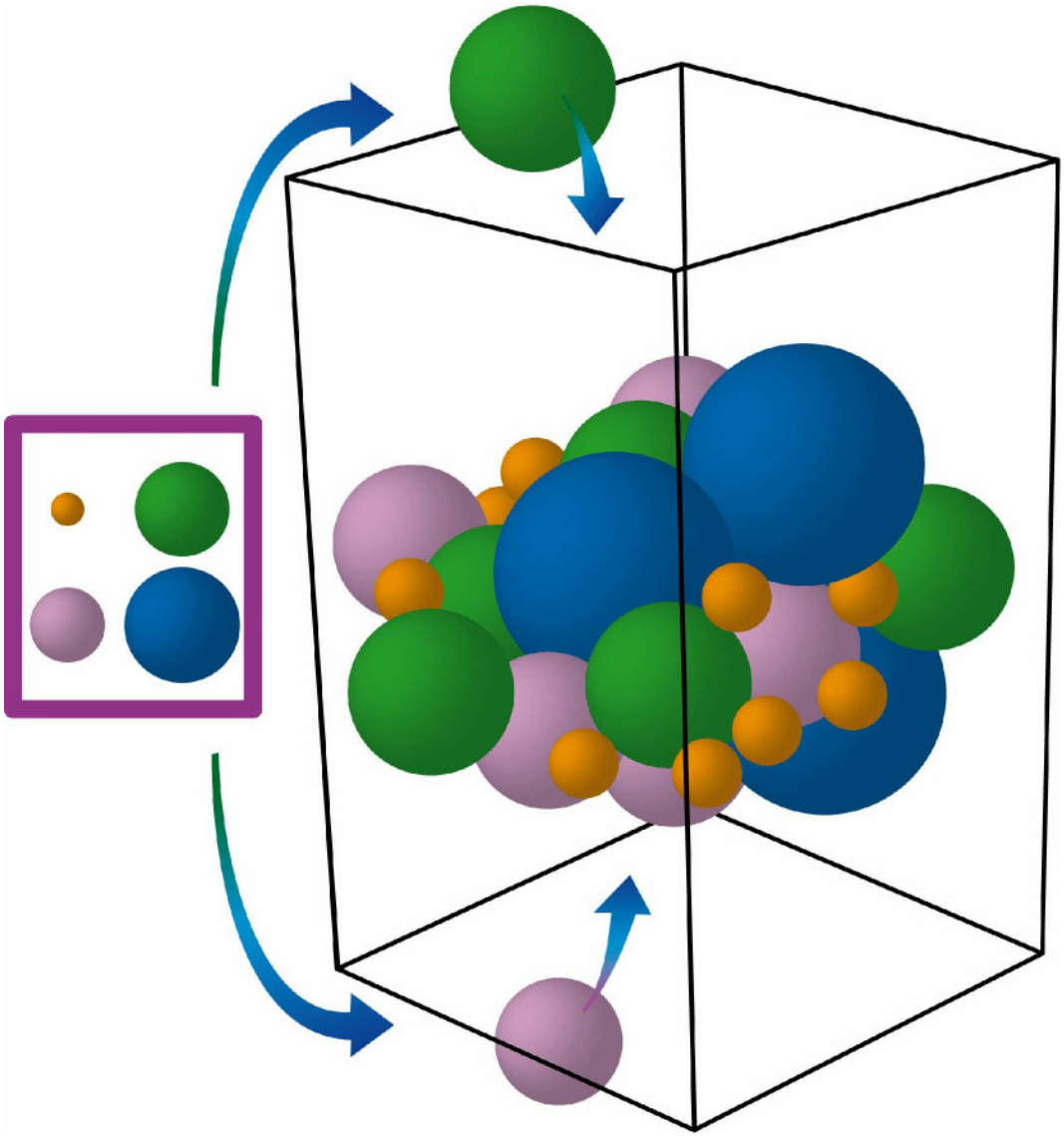

Figure 2: Schematic illustrating the nanoparticle assembly strategy using four nanosphere sizes.

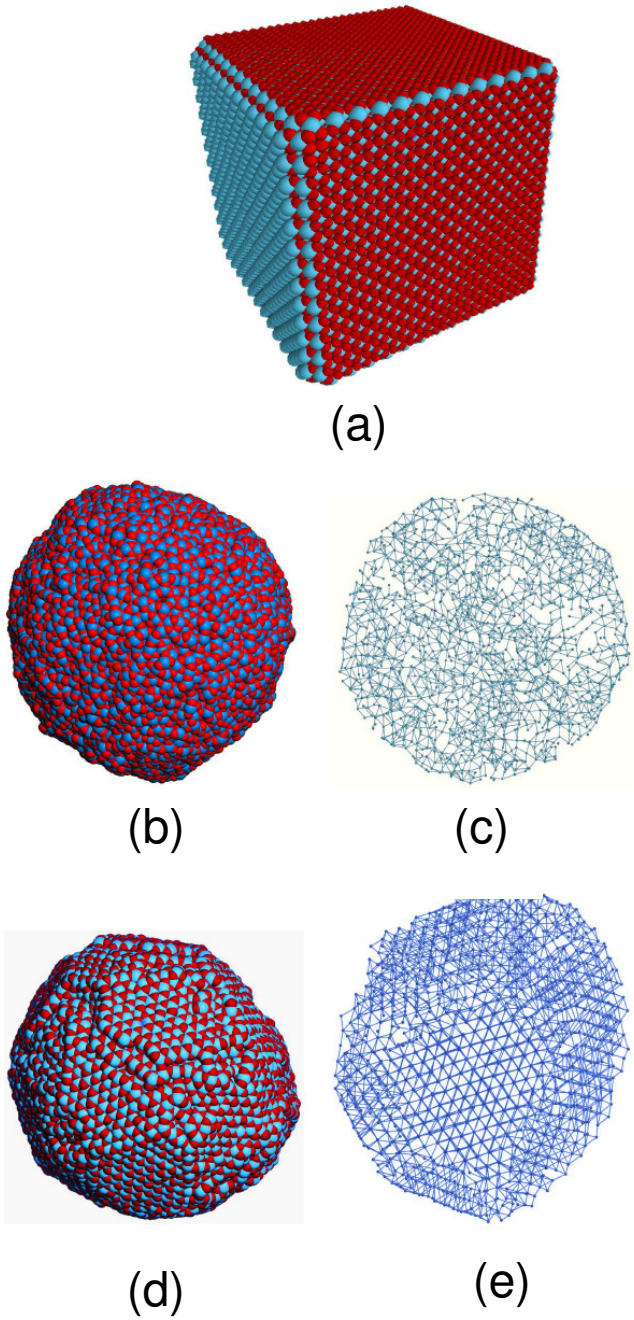

Figure 3: Stages corresponding to the amorphisation and crystallisation of a nanoparticle (PseudoGas not shown). (a) Perfect fluorite-structured cube of UO_2, with cleaved edges. (b) and (c) show a molten nanoparticle. (d) and (e) show the crystallised nanoparticle. (c) and (e) comprise a thin slice cut through the nanoparticle; only uranium atoms are shown to improve clarity. U is coloured blue and O is red.

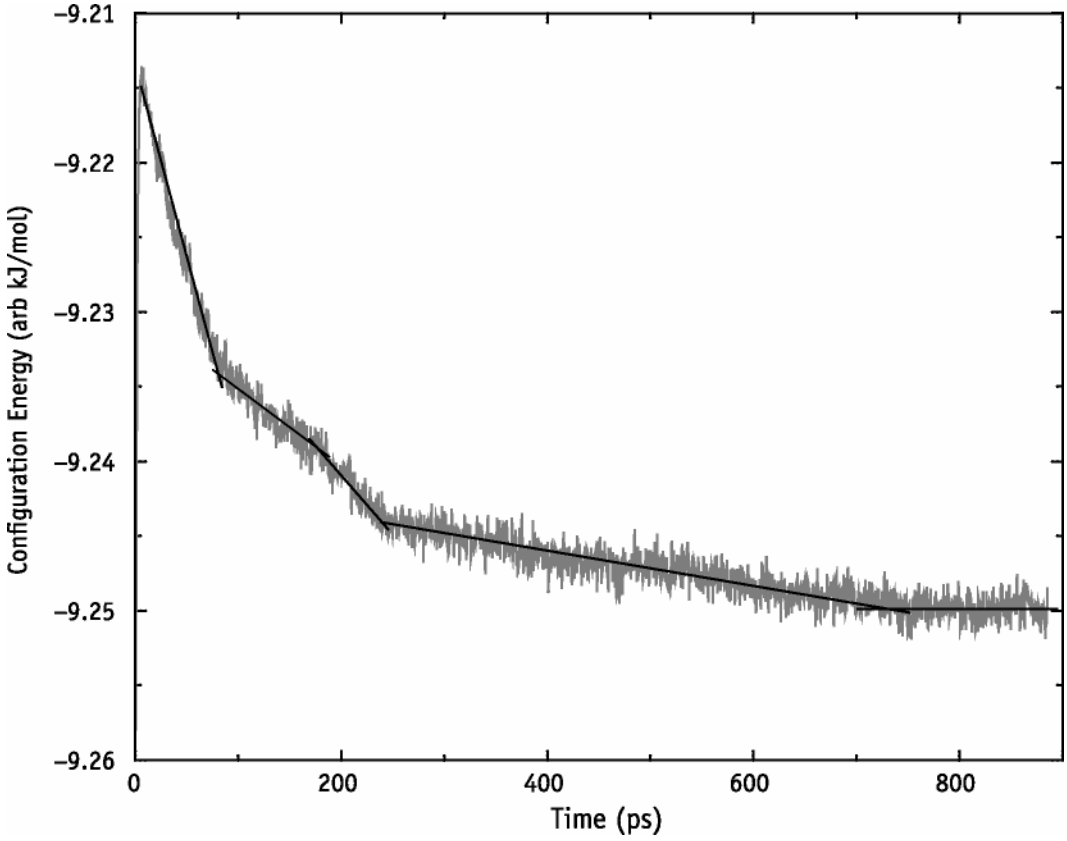

Figure 4: Configuration energy, calculated as a function of time.

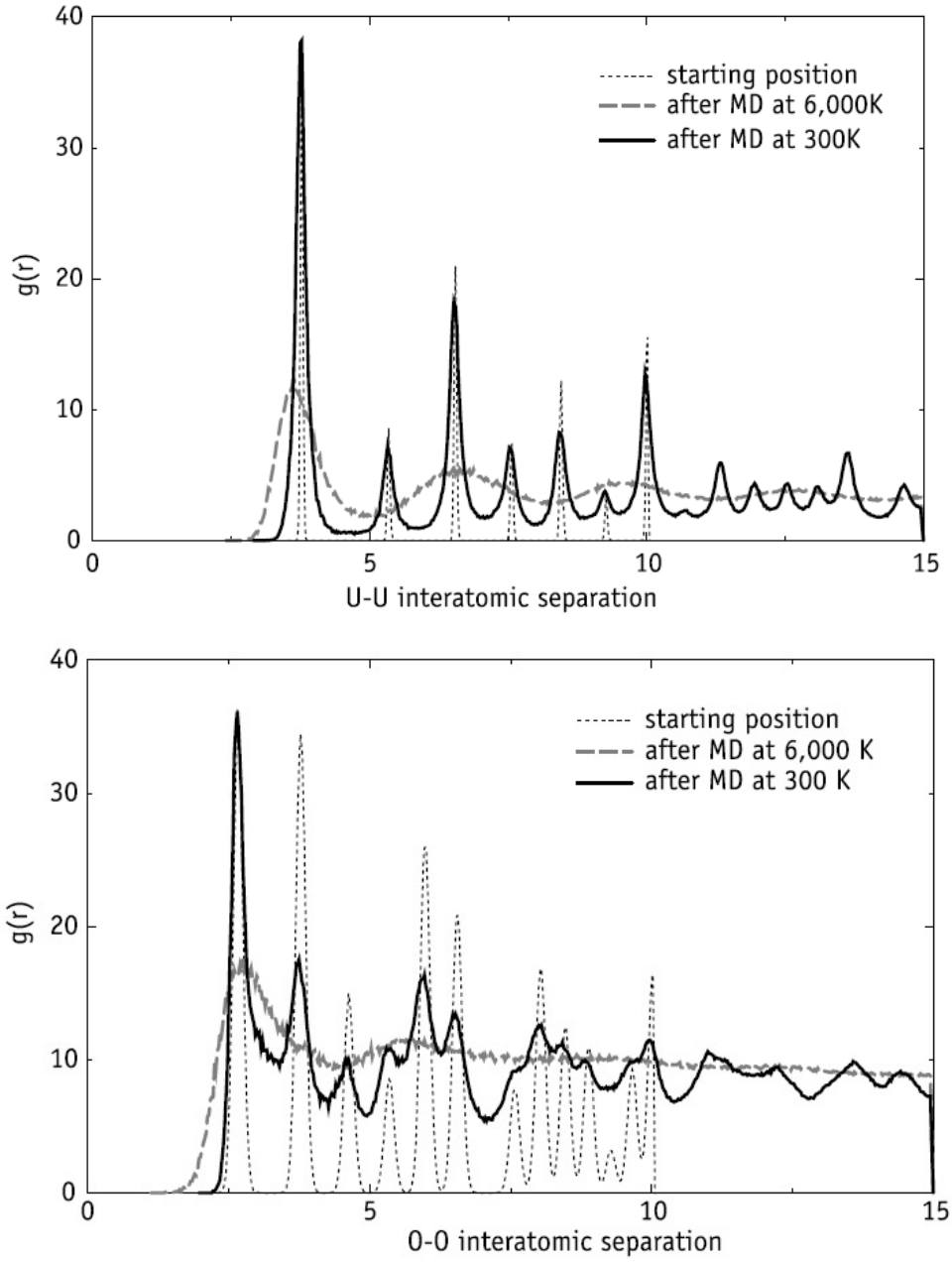

Figure 5: Radial Distribution Functions (RDF), calculated at various stages during the simulation.

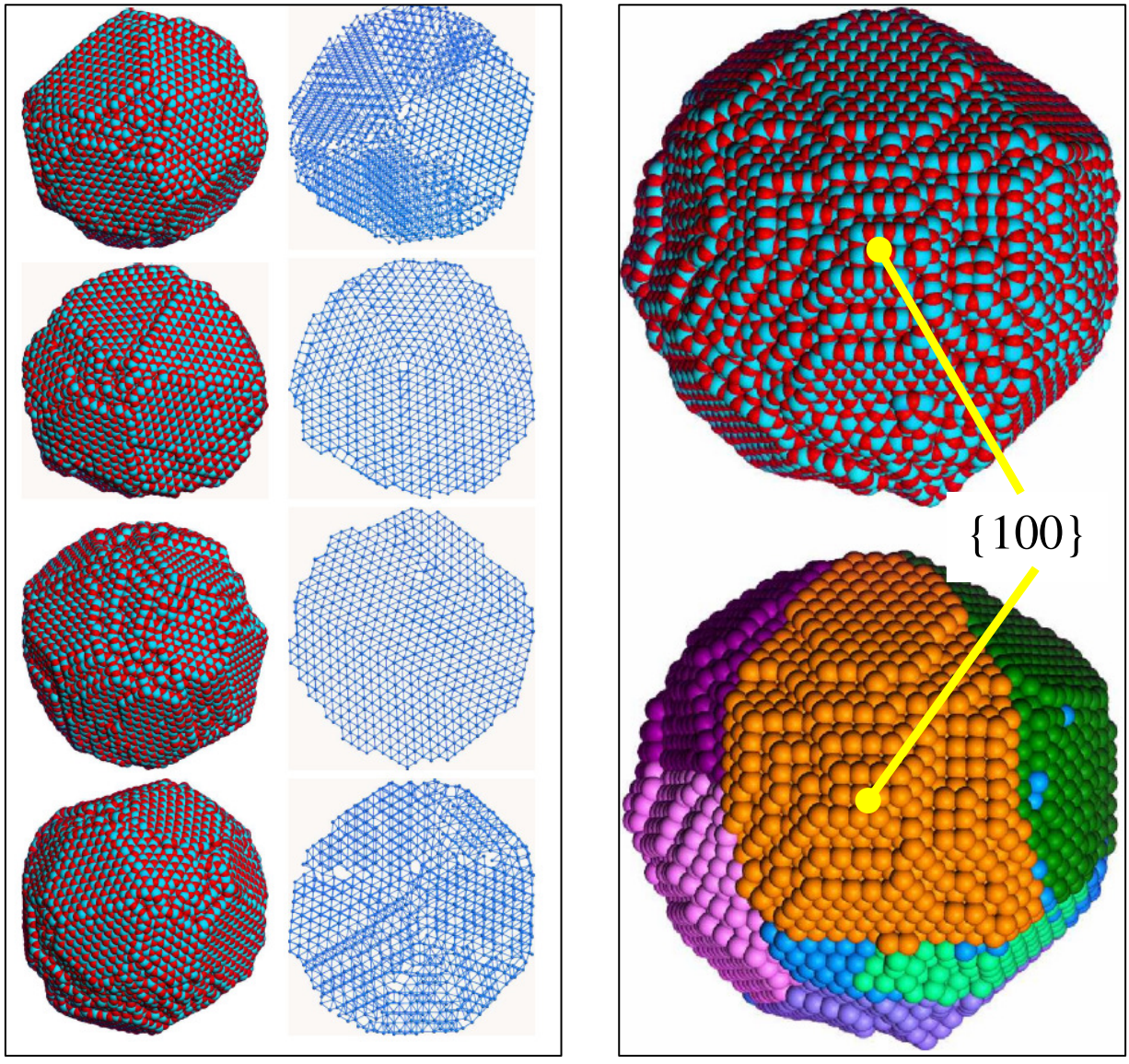

Figure 6: Atomistic structures of UO_2 nanoparticles, each about 9 nm in diameter and comprising 26,364 atoms. U is coloured blue and O is red. (a) four nanoparticles, taken from the library, showing a clear (statistical) structural distribution of nanoparticles. Figures to the left are shown using a sphere model representation of the atom positions, while the corresponding structures to the right show a slice cut through the nanoparticle to reveal more clearly that the nanoparticles are not single crystals; rather they comprise many miss-oriented grains. (b) enlarged nanoparticle revealing more clearly the surface facets – particularly {111} surfaces; the colours of the lower figure (b) label the different grains comprising the nanoparticle.

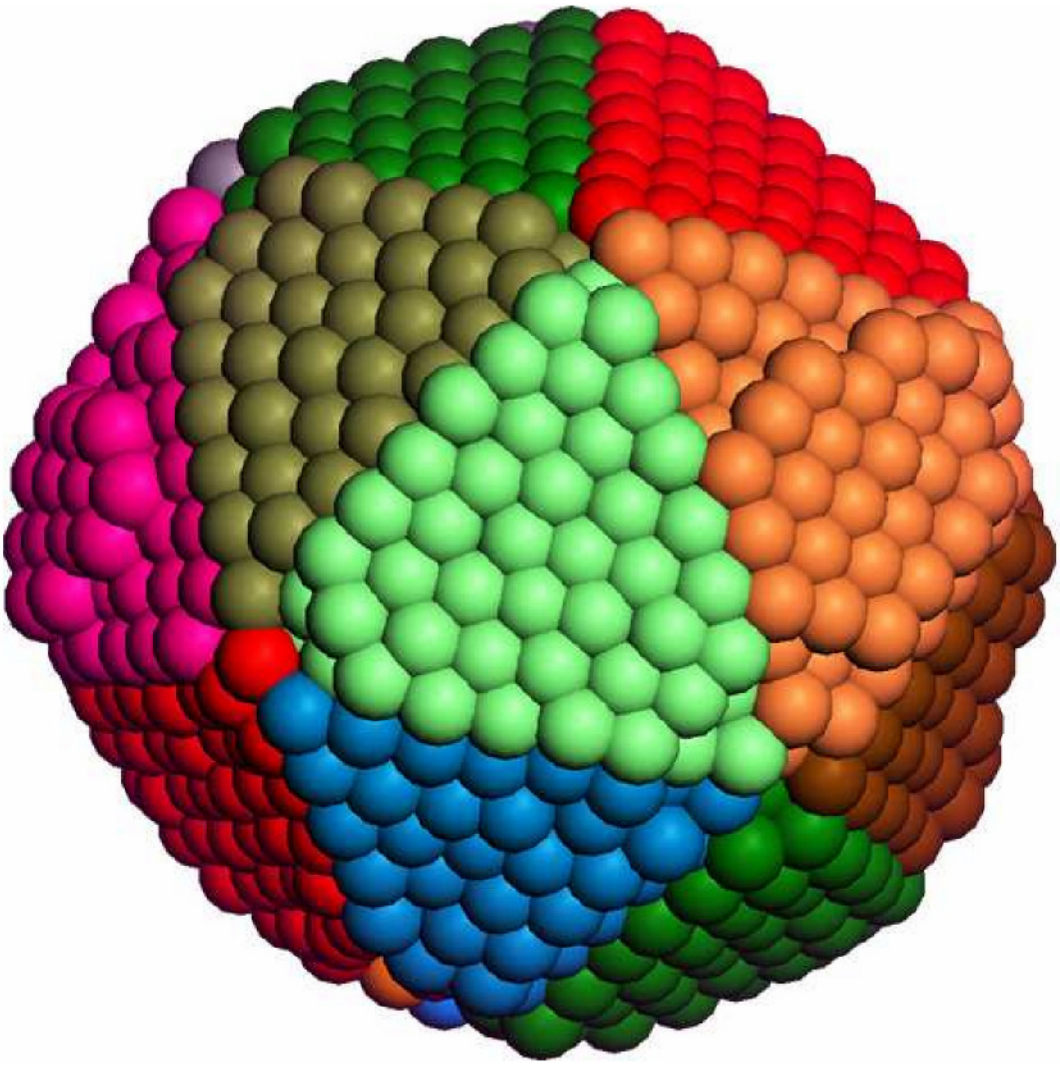

Figure 7: Sphere model representation of the atom positions of a (near perfect) icosahedral UO_2 nanoparticle, which comprises 6,144 atoms and is about 5 nm in diameter. Colour notation is used to label the individual grains. The spheres represent the U atom positions; O atoms are not shown.

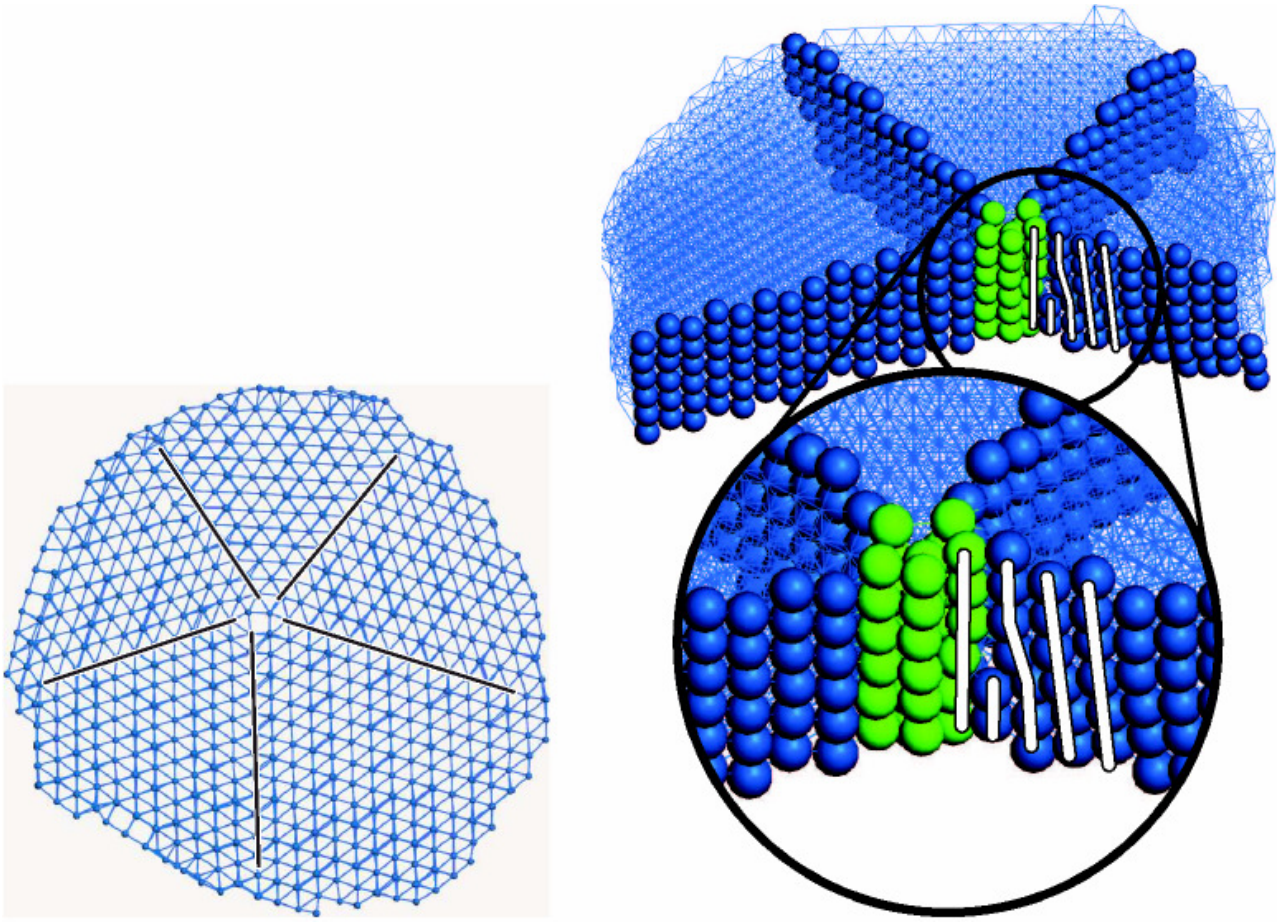

(a) (b)

Figure 8: Representation of a 9 nm UO_2 nanoparticle that comprises five grains, which orient around a central core. Only uranium atom positions are shown to improve clarity. (a) Ball and stick model of the atom positions comprising a thin slice cut through the nanocrystals, the lines show the grain boundaries which terminate at the core. (b) Oriented and cut away view of the nanocrystal revealing the grain-boundaries and the structure of the central core region. The lines highlight an edge dislocation within one of the miss-oriented crystallites.

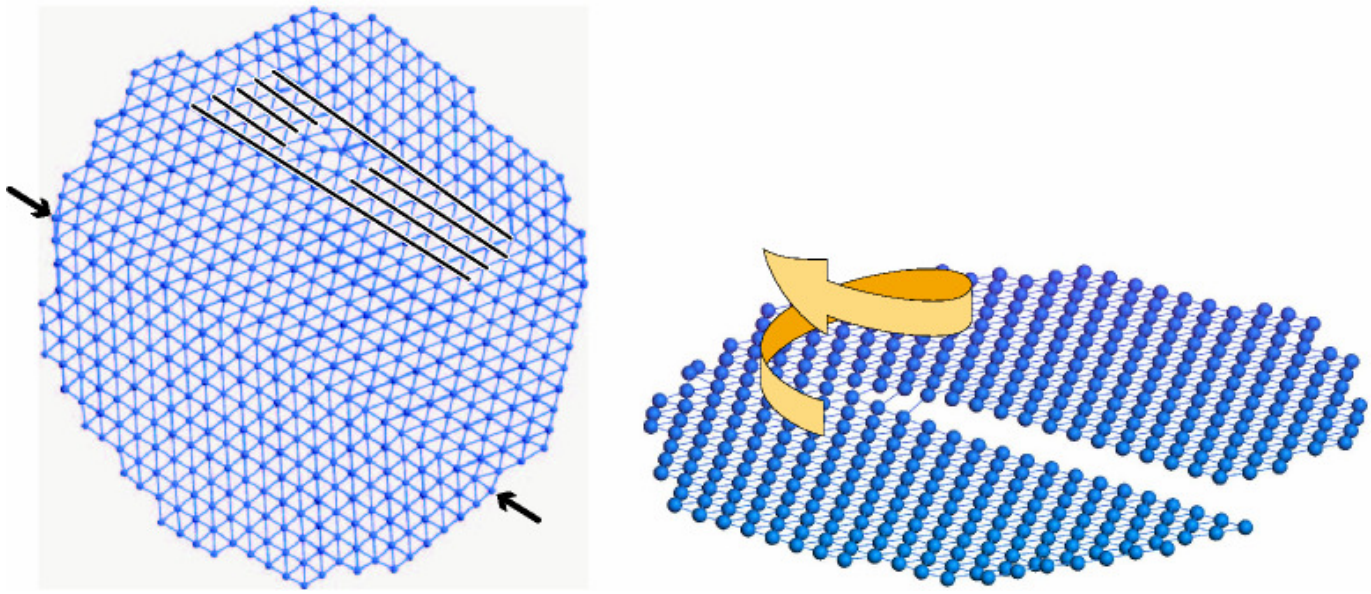

(a) (b)

Figure 9: Representation of the atom positions comprising a slice cut through a 9 nm UO_2 nanoparticle, which comprises a mixed screw-edge dislocation. (a) Edge component to the dislocation is indicated by the lines; the arrows locate the grain boundary. (b) Shows more clearly the screw (clockwise) character of the dislocation. Only uranium atoms are shown to improve clarity of the figure.

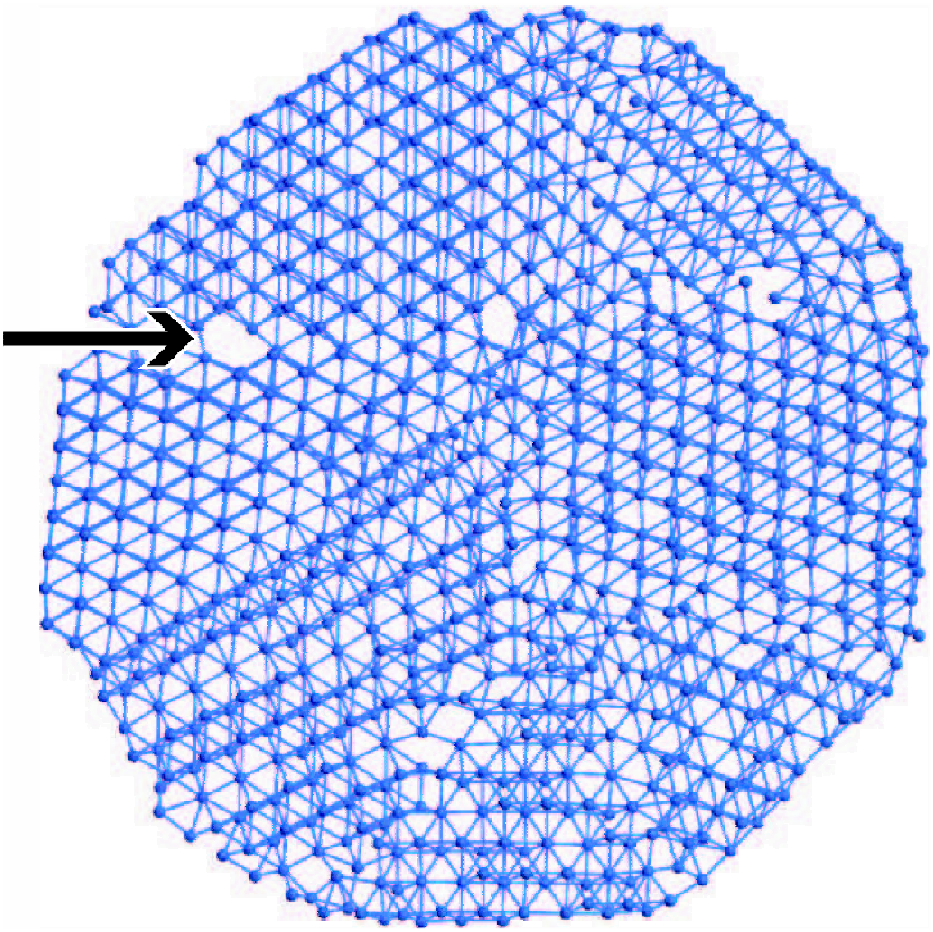

Figure 10: Ball and stick model of the atom positions comprising a slice cut through a 9 nm UO_2 nanoparticle. The arrow indicates a uranium vacancy, which pins a dislocation.

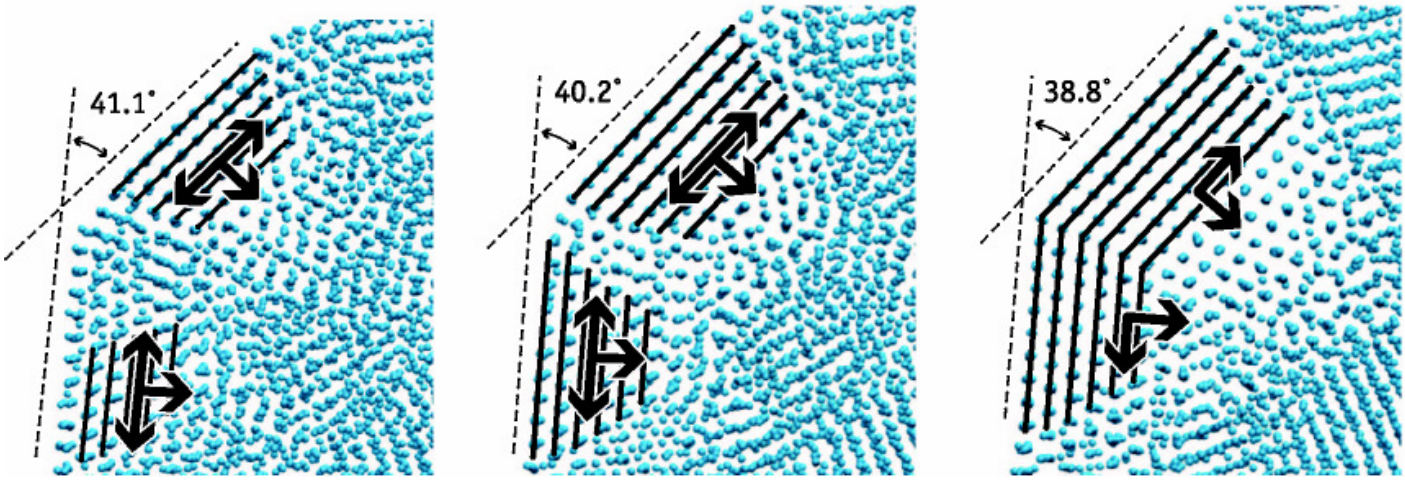

Figure 11: Atomistic structure of a 14 nm UO_2 nanoparticle during crystallisation. Only the uranium atoms are shown for clarity. The lines indicate atomic planes comprising the grains, and the arrows show the growth direction. (a) After 135 ps; (b) 152 ps; (c) 450 ps.

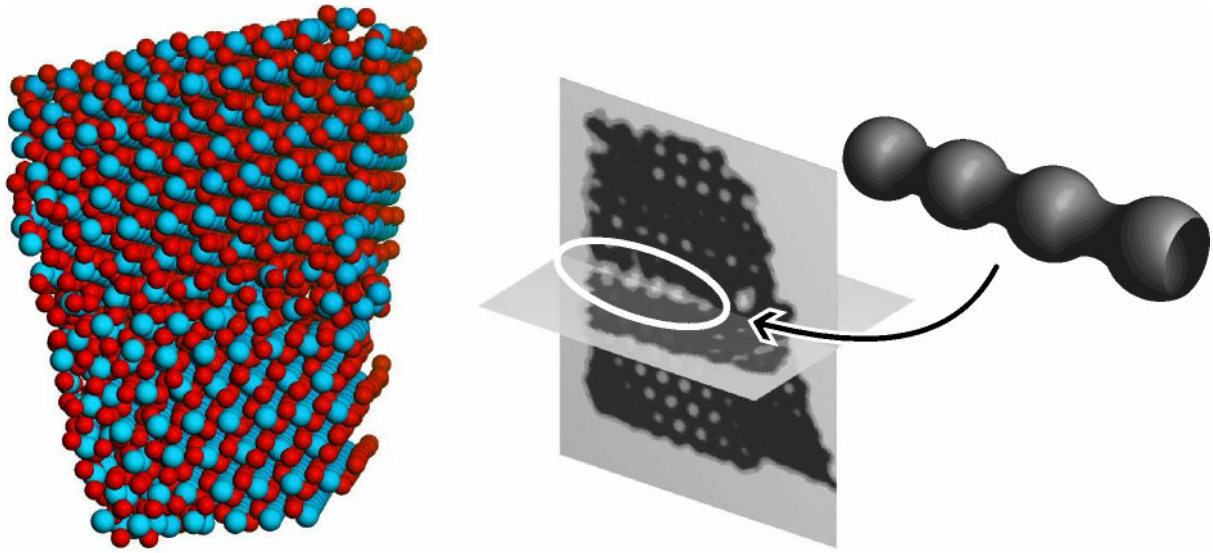

Figure 12: Atomistic structure of a grain boundary. (a) Sphere model representation of the atom positions; U is coloured blue and O is red. (b) Slice through the atomic density (calculated using a Connoly surface algorithm); light grey indicates low density. On the right, a schematic of the channel of low density that can be found between the two grains is shown.

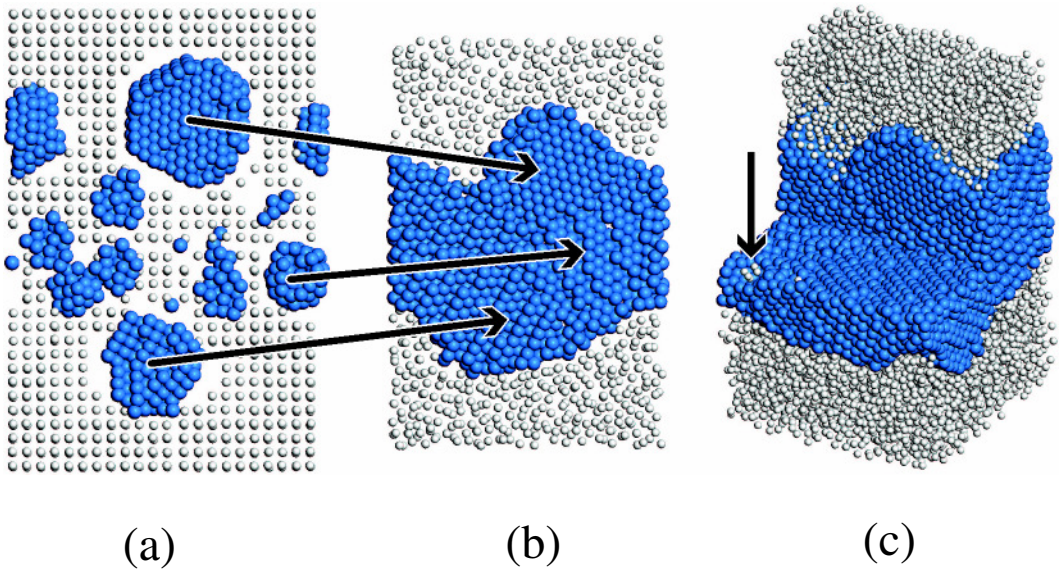

Figure 13: Simulation cell at the start of the simulation, and after 392 ps of MD simulation. (a) Vertical slice cut through the simulation cell revealing the individual nanoparticles. (b) After 392 ps; the arrows indicate the final positions of the nanoparticles shown in (a). (c) Perspective view of the simulation cell after 392 ps; a quarter of the cell has been cut away for clarity. The arrow in (c) highlights the position of trapped PseudoGas atoms, which facilitate void space in the thin film.

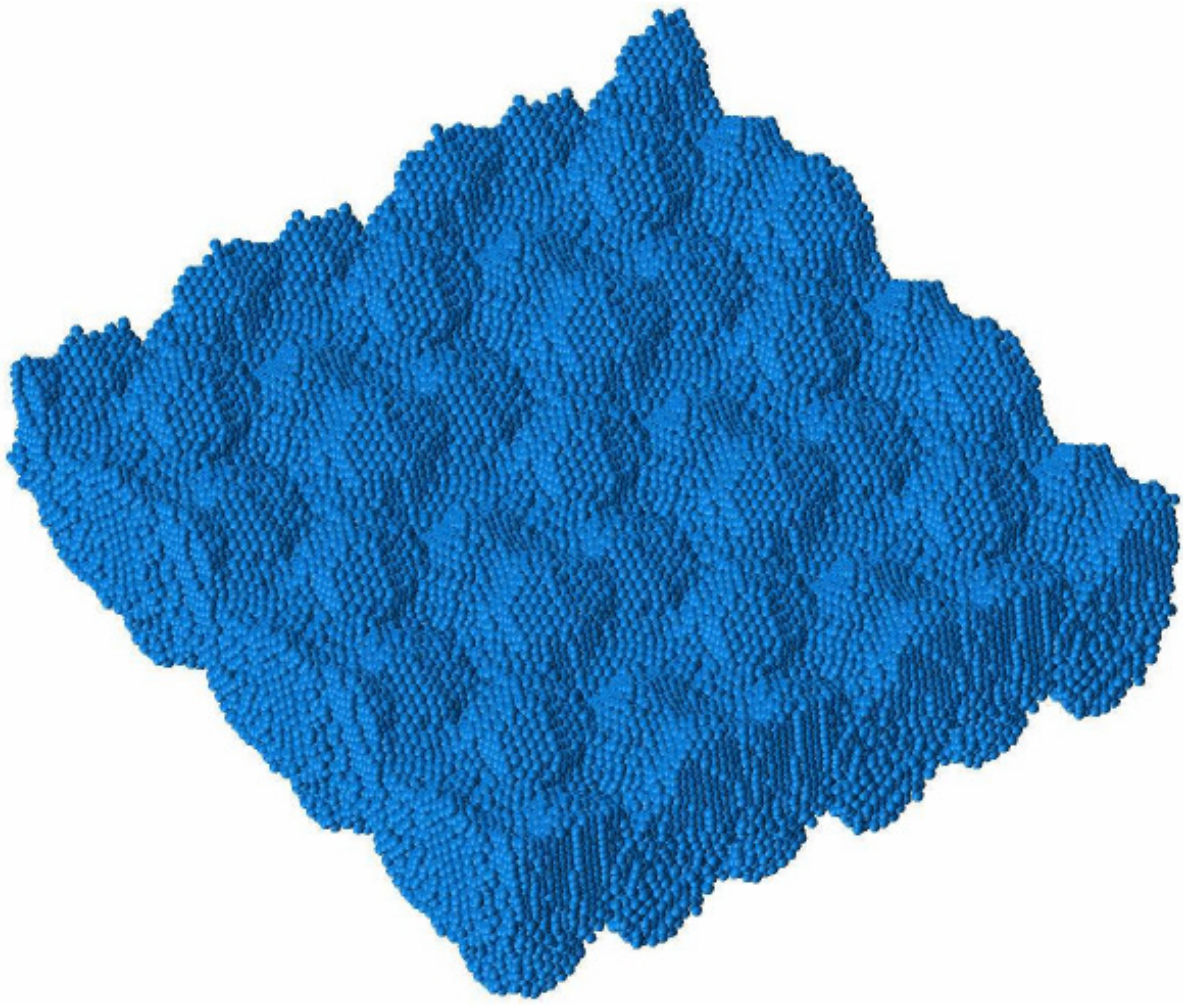

Figure 14: Nanopolycrystalline UO_2 thin film (3 × 3 simulation cells); perspective view looking at the surface of the film. Only uranium atoms are shown to preserve clarity

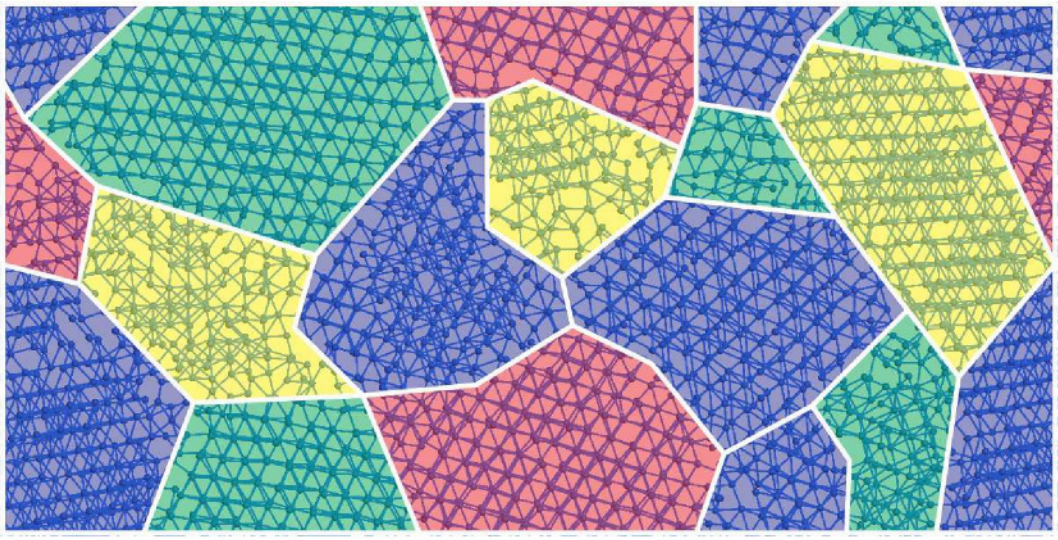

Figure 15: Ball and stick model of the atom positions within a slice cut through the polycrystalline UO_2 bulk. The individual miss-oriented grains are shaded. Only the uranium atoms are shown to improve clarity.

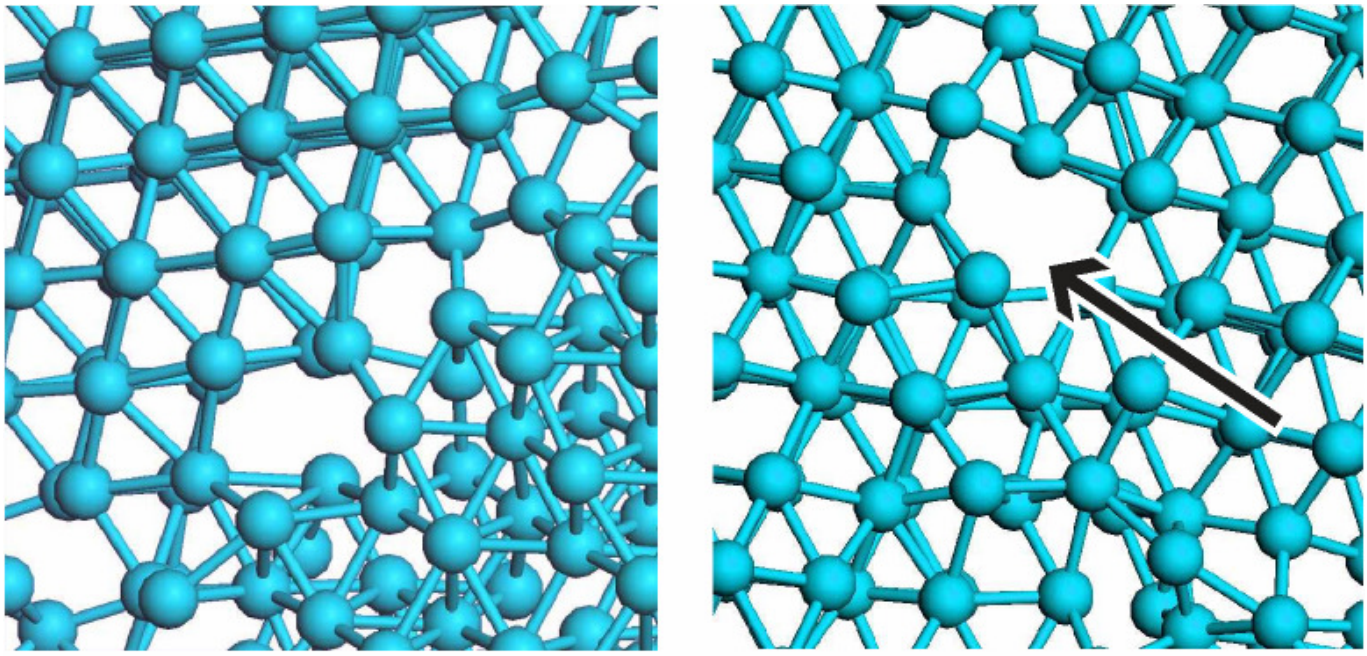

Figure 16: Microstructural features within the polycrystalline UO_2 model. (a) Atomistic structure of a grain-boundary. (b) Atomistic structure of an edge dislocation (arrow). The uranium atom positions are shown using a ball and stick representation; oxygen ions are not shown to preserve clarity.

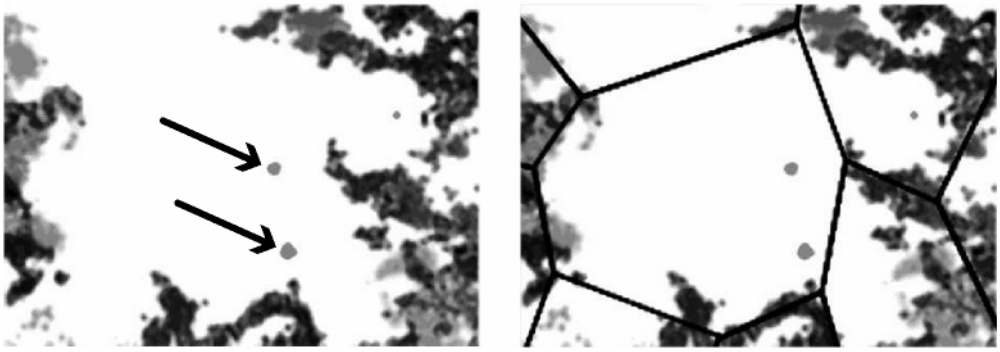

(a) (b)

Figure 17: Helium diffusion profile in the polycrystalline UO_2 matrix. The trajectories of different He atom trajectories are shown using grey-scale. The arrows in the middle of (a) indicate two He atoms, which are trapped inside a UO_2 grain. The other atoms diffuse faster and are associated with longer trails. The lines in (b) indicate the positions of the grain boundaries. We note that the images are three dimensional and therefore the trajectories can be above or below the plane of the page.

REFERENCES

[1] Sayle, T. X. T.; Catlow, C.R.A.; Sayle, D.C.; Parker S.C. and Harding. J.H. *Phil. Mag. A* 1993, 68, 565-573.

[2] Abrefah, J.; Huang, F. H.; Gerry, W. M.; Gray, W. J.; Marschman, S. C.; Thornton, T. A. *Analysis of Ignition Testing on K-West Basin Fuel; PNNL 11916 UC 602* Technical Report, 1999.

[3] Totemeier, T. C.; Hayes, S. L. *Analytical and Numerical Models of Uranium ignition assisted by Hydride formation;* ANL/ED/CP--88016; CONF-9606116—15, OSTI ID: 238467 **1996**.

[4] Baker, M. M; Less, L. N.; Orman, S. *Trans. Faraday Soc.*, **1966**, 62, 2513 - 2524

[5] Wood, D. H.; Snowden, S. A.; Howe, H. J.; Thomas, L.; Moon, D. W.; Gregg, H. R.; Miller, P. E. *Journal of Nuclear Materials* **1994,** *209,* 113–115.

[6] Walker, J. R.; Catlow, C. R. A. *Journal of physics C: Solid State Physics* **1981,** *14,* 979–983.

[7] Kurosaki, K.; Yamada, K.; Uno, M.; Yamanaka, S.; Yamamoto, K. *Journal of Nuclear Materials* **2001**,*294***,** 160–167.

[8] Idiri, M.; Le Bihan, T.; Heathman, S.; Rebizant, J. *Physical Review B* **2004,** *70,* 014113.

[9] Grimes, R. W.; Miller, R. H.; Catlow, C. R. A. *Journal of Nuclear Materials* **1990,** *172,* 123–125.

[10] Ball, R. G. J.; Grimes, R. W. *Journal of Chemistry Society, Faraday Transactions* **1990,** *86,* 1257–1261.

[11] Price, D. W. *Discovery* **2006,** *9,* 18–27.

[12] Duffy, D. M.; Tasker, P. W. *Physica B+C* **1985,** *131,* 46–52.

[13] Duffy, D. M.; Tasker, P. W. *Phil. Mag. A* **1986**,*54***,** 759–771.

[14] Harding, J. H. *Rep. Prog. Phys.* **1990**,*53***,** 1403–1466.

[15] Watson, G. M.; Gibbs, D.; Lander, G. H.; Gaulin, B. D.; Berman, L. E.; Matzke, H.; Ellis, W. *Physical Review Letters* **1996,** *77,* 75 1–755.

[16] Schiotz, J.; Di Tolla, F. D.; Jacobson, K. W. *Nature* **1998,** *391,* 561–561.

[17] Phillpot, S. R.; Keblinski, P.; Wolf, D.; Cleri, F. *Interface Science* **1999,** *7,* 15–3 1.

[18] Sayle, D. C.; Johnston, R. L. *Current Opinion in Solid State & Materials Science* **2003,** *7,* 3–12.

[19] Sayle, D. C.; Watson, G. W. *Journal of Materials Chemistry* **2000,** *10,* 2241–2243.

[20] Sayle, D. C.; Seal, S.; Wang, Z.; Mangili, B. C.; Price, D. W.; Karakoti, A. S.; Kuchibhatla, S. V. T. N.; Hao, Q.; Möbus, G.; Xu, X.; Sayle, T. X. T. *ACS Nano* **2008,** *2,* 1237–1251.

[21] Wolf, D.; Yamakov, V.; Phillpot, S. R.; Mukherjee, A.; Gleiter, H. *Acta Materiala* **2005,** *53,* 1–40.

[22] Sutton, A. P.; Balluffi, R. W. *Interfaces in Crystalline Materials.;* Clarenden Press, Oxford, 1995.

[23] Smith, W.; Forester, T. R. *Journal of Molecular Graphics* **1996,** *14,* 136–141.

[24] Wang, Q.; Li, G.-D.; Xu, S.; Li, J.-X.; Chen, J.-S. *Journal of Materials Chemistry* **2008,** *18,* 1146–1152.

[25] Dickey, E. C.; Fan, X. D.; Pennycook, S. J. *J. Am. Ceram. Soc.* **2001,** *84,* 1361–1368.

[26] Sayle, D. C.; Maicaneanu, S. A.; Watson, G. W. *Journal of the American Chemical Society* **2002,** *124,* 11429–11439.

[27] Walker, A. M.; Slater, B.; Gale, J. D.; Wright, K. *Nature Materials* **2004,** *3,* 7 15–720.

[28] Piana, S.; Gale, J. D. *Journal of the American Chemical Society* **2005,** *127,* 1975–1982.

[29] Hamad, S.; Catlow, C. R. A. *Journal of Crystal Growth* **2006,** *294,* 2–8.

[30] Sayle, D. C.; Feng, X. D.; Ding, Y.; Wang, Z. L.; Sayle, T. X. T. *Journal of the American Chemical Society* **2007,** *129,* 7924–7935.

[31] Feng, X. D.; Sayle, D. C.; Wang, Z. L.; Paras, M. S.; Santora, B.; Sutorik, A. C.; Sayle, T.X. T.; Yang, Y.; Ding, Y.; Wang, X.; Her, Y.-S. *Science* **2006**,*312***,** 1504–1508.

[32] Sayle, T. X. T.; Parker, S. C.; Sayle, D. C. *Chem. Commun.* **2004,** 2438–2439.

[33] Tasker, P. W. *Surface Science* **1979,** *78,* 3 15–324.

[34] Sayle, D. C.; Sayle, T. X. T. *Journal of Computational and Theoretical Nanoscience* **2007**,*4***,** 299–308.

[35] Melchionna, S.; Ciccotti, G.; Holian, B. L. *Molecular Physics* **1993,** *78,* 533.

[36] Kang, K. H.; Ryu, H. J.; Song, K. C.; Yang, M. S. *Journal of Nuclear Materials* **2002,** *301,* 242–244.

[37] Kupryazhkin, A. Y.; Zhiganov, A. N.; Risovany, D. V.; Nekrassov, K. A.; Risonavy, V. D.; Golovanov, V. N. *Journal of Nuclear Materials* **2008,** *372,* 233–238.

[38] Zhang, H. Z.; Gilbert, B.; Huang, F.; Banfield, J. F. *Nature* **2003**,*424***,** 1025–1029.

[39] Stanek, C. R.; Bradford, M. R. and Grimes, R. W., *J. Phys. Condens. Matter.* **2004**, 16, S2699–S2714

[40] Khan, M.S.; Islam, M. S. and Bates, D. R., J. Mater. Chem., **1998**, 8, 2299-2307**.**

[41] Sayle, D. C.; Doig, J. A.; Parker, S. C.; Watson, G. W.; Sayle, T. X. T. *Phys. Chem. Chem. Phys.* **2005,** *7,* 16–18.

[42] Roudil, D.; Deschanels, X.; Trocellier, P.; Jégou, C.; Peuget, S.; Bart, J.-M. *Journal of Nuclear Materials* **2004,** *325,* 148–158.

[43] Kadau, K.; Germann, T. C.; Lomdahl, P. S.; Holian, B. L.; Kadau, D.; Entel, P.; Kreth, M.; Westerhoff, F.; Wolf, D. *Metallurgical and Materials Transactions A* **2004**,*35***,** 2719.

[44] Catlow, C. R. A.; Faux, I. D.; Norgett, M. J. *Journal of physics C: Solid State Physics* **1976,** *9,* 419–429.

[45] Paszti, F. *Nuclear Instruments and Methods in Physics Research B* **1992,** *66,* 83–106.

[46] Guilbert, S.; Sauvage, T.; Garcia, P.; Carlot, G.; Barthe, M.-F.; Desgardin, P.; Blondiaux, G.; Corbel, C.; Piron, J. P.; Gras, J.-M. *Journal of Nuclear Materials* **2004,** *327,* 88–96.

[47] Sauvage, T.; Desgardin, P.; Martin, G.; Garcia, P.; Carlot, G.; Labrim, H.; Khodja, H.; Moretto, P.; Barthe, M.-F.; Blondiaux, G.; Erramli, H.; Piron, J. P. *Nuclear Instruments and Methods in Physics Research B* **2005**,*240***,** 27

[48] Yun, Y.; Eriksson, O. and Oppeneer, P. M., *J. Nucl. Mater.* 2009, 385, 510-516